3D Simulation of Cell Design Influences on Sodium–Iodine Battery Performance

Felix Gerbig,* Susanne Cernak, and Hermann Nirschl

This publication deals with the spatially resolved simulation of a sodium–iodine secondary battery. The anode compartment consists of molten sodium and the cathode compartment contains a high-conductivity metal disc as electrode and an aqueous catholyte. The latter comprises iodide, triiodide, dissolved iodine, and sodium ions. A finite volume approach is proposed to model the transport processes and electrochemical reactions focusing on the positive half-cell. The study investigates the influences of cathode length, C-rate, electric conductivity, and molar concentrations on cell performance. It considers solubility limits and predicts diffusion limitation as the major constraint for the operating window. The presented investigations are confined to a simple cathode geometry. However, the results demonstrate the capability of the model to design sodium–iodine half-cells.

1. Introduction

High-temperature liquid sodium batteries (e.g., sodium–sulfur batteries) are a well-established technology for large-scale grid storage. Combining the molten sodium anode with an aqueous iodine cathode overcomes the problems of thermal losses and sealing by reducing the operating temperature to about 100 °C. This leads to a higher cost efficiency and energy density, and a simplified cell design.

Recent research urges to develop batteries using naturally abundant materials while maintaining cost-effectiveness.[1] Due to their sustainability and high efficiency, which are comparable to the respective values of lithium-ion batteries, midtemperature sodium–iodine batteries are promising candidates for small- and medium-scale stationary energy storage applications. Sodium is an inexpensive, relatively nonhazardous and easy-to-handle material, which is available in large amounts. Its use as a molten anode and its application in sodium-ion batteries have therefore been in the focus of research for a long time.[2,3]

F. Gerbig, S. Cernak, Prof. H. Nirschl
Institute of Mechanical Process Engineering and Mechanics
Karlsruhe Institute of Technology
Strasse am Forum 8, 76131 Karlsruhe, Germany
E-mail: felix.gerbig@kit.edu

The ORCID identification number(s) for the author(s) of this article can be found under https://doi.org/10.1002/ente.202000857.

Sodium–sulfur batteries, developed in the 1980s, use molten sulfur as the positive electrode at temperatures of around 300 °C.[4,5] From there, the so-called ZEBRA battery evolved, which contains a solid nickel chloride electrode in addition to a liquid electrolyte (sodium chloroaluminate).[6] It reduces the minimum operating temperature to 157 °C. The sodium–iodine battery temperature is solely limited to the melting point of sodium when using an aqueous solution for the positive electrode. Experiments performed by Holzapfel et al. show proof-of-principle for a current density of 20 mA cm^{-2} (55 mW cm^{-2}) up to a maximum current density of 100 mA cm^{-2} (180 mW cm^{-2}).[7] The used iodine concentrations correspond to 405 Wh L^{-1} on a catholyte basis or 198 Wh kg^{-1} including anolyte and catholyte, which is comparable to commercialized lithium-ion batteries. Sodium–iodine batteries have the ability to meet the growing demand for energy storage caused by the integration of renewable energy sources into the power grid.

Although these batteries are theoretically described in the literature,[8] the detailed processes inside the battery are not well understood. Quantities like initial species concentrations, C-rate, cell design, and cathode geometry have large impacts on the overall battery performance. As experimental studies are limited to macroscopic quantities like electronic current and potential, a fully resolved 3D simulation model is set up to gain insights into microstructural processes inside the battery.

Simulation methods for applications in battery research apply to different time and length scales. The proposed model lines up in the category of macroscopic models following the classification for lithium-ion simulation methods proposed by Shi et al.[9] The model resolves the electrode and cell level and is based on continuum hypothesis. The objective is to address macroscale phenomena by exploring microstructural influences like geometrical properties on voltage and concentration distribution throughout the whole charging process.

A variety of spatially resolved continuum models exists for Li-ion batteries.[10] First, a microstructural model was introduced and then extended to three dimensions by Garcia et al.[11,12] Goldin et al. and Less et al. used 3D models to investigate particle influences.[13,14] Wang and Sastry evaluated lithium diffusivities by fitting simulated discharge curves and implementing a spatially resolved model in a commercial software package.[15] Wiedemann et al. reconstructed lithium-ion battery cathode structures from focused-ion-beam scanning electron microscopy experiments and found significant 3D spatial lithium

ADVANCED
SCIENCE NEWS
www.advancedsciencenews.com

Energy Technology
Generation, Conversion, Storage, Distribution
www.entechnol.de

concentration variations.[16] Kespe et al. developed a 3D simulation model for lithium manganese oxide as well as blended cathodes, and precisely described cell performance and behavior.[17–19] Cernak et al. used the same model to investigate the influence of lithium nickel manganese cobalt oxide particle roughness on electrochemical performance.[20] Latz and Zausch compare a resolved model with homogenized theory in thermal–electrochemical lithium-ion battery simulations.[21,22] They observe strong local fluctuations on the microscale. All authors showed that spatially resolved microstructure models are well suited for investigating geometrical influences within battery cells.

Zhu and Kee[8] indicated that exceeding solubility limits or depletion of reacting species define the operating window of a sodium iodine battery. This publication continues the research on aqueous sodium iodine batteries by setting up a 3D simulation model. The spatially resolved model allows describing cathode geometry precisely and prospecting the local distribution of ion species, which is crucial for determining operating limits.

2. Mathematical and Numerical Model

The following section states the thermodynamics of a liquid sodium–iodine secondary battery. The electrochemical model builds up on the 1D model established by Zhu and Kee[8] and is described in detail there. The underlying basic thermodynamics are textbook knowledge.[23–25] Nevertheless, this section presents the governing equations, which are necessary to understand the additions for implementing these thermodynamics in a spatially resolved simulation model. It is based on charge and species conservation throughout all computational domains. The anode compartment is filled with molten sodium that has a very high electric conductivity and, therefore, a small contribution to the cell voltage. The present model focuses on the cathode half-cell, thus not resolving the anode half-cell.
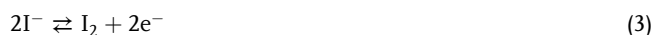
Equation (1) denotes the net reaction. During discharging, elemental sodium oxidizes to sodium ions, while iodine is reduced to iodide at a standard potential of 3.2495 V.

$$2Na^+ + 2I^- \rightleftarrows I_2 + 2Na \tag{1}$$

The half-cell reaction for the negative electrode states

$$Na^+ + e^- \rightleftarrows Na \tag{2}$$

at standard potential -2.714 V against hydrogen electrode, while it is

$$2I^- \rightleftarrows I_2 + 2e^- \tag{3}$$

for the positive half-cell ($E^\circ = 0.5355$).[26,27]

The discharge process consumes elemental sodium at the anode–separator interface causing the amount of sodium in the anode compartment to decrease. NASICON serves as separator. NASICON is a ceramic material that is a pure ion conductor for sodium ions with high ionic conductivity.[28] The interfacial resistance between NASICON and molten sodium is very low when coating the NASICON surface with tin or SiO_2.[29,30] It may be long-term resistant to aqueous solutions.[31]

Figure 1 shows the working principle of the battery. At discharge, sodium ions form in the molten sodium anode at the
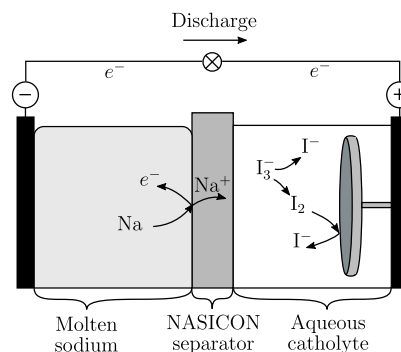

Figure 1. Working principle of sodium–iodine battery.

anode–separator interface, travel through the separator, and enter the cathode domain. The cathode domain comprises I_2, I^-, I_3^-, and Na^+ dissolved in water. Iodide forms at the electrolyte–cathode electrode interface from iodine and electrons delivered by the external current. Iodine itself has a low solubility in water but can homogeneously recombine to triiodide with iodide. I^-/I_3^- is an interesting redox couple due to its high solubility in aqueous solutions, low molecular weight, and high faradaic efficiency.

2.1. Species Transport

The species transport equation derives from mass conservation considering surface fluxes and molar production rates.

$$\frac{\partial [X_k]}{\partial t} = -\nabla \cdot \mathbf{J_k} + r_k \tag{4}$$

The surface fluxes $\mathbf{J_k}$ contain a diffusion component and migration component in a Nernst–Planck formulation that is estimated based on dilute solution theory.[8,32]

$$\mathbf{J_k} = -D_k^{el} \nabla [X_k] - \frac{z_k F}{RT} D_k^{el} [X_k] \nabla \Phi_{el} \tag{5}$$

Based on measurements by Wroblowa and Saunders,[33] triiodide decomposition happens in a three-step mechanism with the adsorption (step 3) being the rate-determining step

$$I_3^- \rightleftarrows I_2 + I^- \tag{6}$$

$$I_2 \rightleftarrows 2I_{ads} \tag{7}$$

$$e^- + I_{ads} \rightleftarrows I^- \tag{8}$$

The reaction kinetics of the heterogeneous reaction determined by reaction 3 are expressed by the exchange current density i_0. Zhu and Kee derive it from the elementary Marcus form of the adsorption step (Equation (8)).[8]

$$i_0 = i^\circ_0 \frac{\left(\frac{[I_2]}{[I_2]^*}\right)^{\frac{\beta_a}{2}} \left(\frac{[I^-]}{[I^-]^*}\right)^{1-\beta_a}}{1 + \left(\frac{[I_2]}{[I_2]^*}\right)^{\frac{1}{2}}} \tag{9}$$

The exchange current density factor i°_0 is a fitting parameter to match experimental data.[34] The reference concentrations $[I_2]^*$

ADVANCED
SCIENCE NEWS

www.advancedsciencenews.com

Energy Technology
Generation, Conversion, Storage, Distribution

www.entechnol.de

and $[I^-]^*$ are set to 1 M. The symmetry factor β_a is 0.5. As an intermediate step, homogeneous triiodide formation may happen in a two-step mechanism with both reactions being of first order,[35] which results in two observable voltammetric waves lying close to each other.[36,37] However, iodide oxidation can be globally described by reaction (3).

It is possible to model triiodide formation in the catholyte with the equilibrium constant K[38]

$$K = \frac{[I_3^-]}{[I^-][I_2]} \tag{10}$$

which is temperature-dependent and has the value

$$K(120\,°C) = 0.121\,\frac{mol}{m^3} \tag{11}$$

at 120 °C. The present model considers the homogeneous reaction via source terms. Triiodide forms via combination of iodine and iodide[39]

$$r_{I_2} = -k_f[I_2][I^-] + \frac{k_f}{K}[I_3^-] = r \tag{12}$$

$$r_{I^-} = -k_f[I_2][I^-] + \frac{k_f}{K}[I_3^-] = r \tag{13}$$

$$r_{I_3^-} = k_f[I_2][I^-] - \frac{k_f}{K}[I_3^-] = -r \tag{14}$$

The reaction constant k_f is simply high because the adsorption process is the rate-determining step. Diffusion coefficients are the bulk diffusion coefficients refitted by Zhu and Kee to the operating temperature.[8,40–42]

It is necessary to introduce boundary conditions for all electrolyte species for the electrolyte–separator interface and for the electrolyte–cathode interface to solve Equation (4). At the electrolyte–cathode interface, sodium ion flux $\mathbf{n} \cdot \mathbf{J_{Na+}}$ vanishes. The electrolyte current density completely transfers into iodide and iodine following the heterogeneous reaction path from Equation (3). At the same time, the homogeneous reaction in Equation (6) takes place to fulfill the demanded equilibrium constant. It is convenient to represent the molar production at the electrolyte–cathode interface, which is caused by the homogeneous reaction as boundary fluxes. The fluxes related to the heterogeneous and homogeneous reactions add to the resulting total boundary flux.

$$\mathbf{n} \cdot \mathbf{J_{k,tot}} = \mathbf{n} \cdot \mathbf{J_{k,het}} + \mathbf{n} \cdot \mathbf{J_{k,hom}} \tag{15}$$

The surface unit normal vector pointing outside the computational domain is $\mathbf{n}$. Iodine almost completely reacts to or is formed from iodide and triiodide because of the high equilibrium constant K. Therefore, the corresponding homogeneous reaction surface fluxes at the cathode electrode are equal.

$$\mathbf{n} \cdot \mathbf{J_{I_2,hom}} \approx \mathbf{n} \cdot \mathbf{J_{I_3^-,hom}} = -\mathbf{n} \cdot \mathbf{J_{I^-,hom}} \tag{16}$$

In total, iodine flux at the electrolyte–cathode interface is zero and all species surface fluxes are dependent on the electrolyte current density. Table 1 shows the related boundary conditions.

Table 1. Electrolyte–cathode interface boundary flux densities related to heterogeneous and homogeneous electrolyte reactions.

X_k	$n \cdot J_{k,het}$	$n \cdot J_{k,hom}$	$n \cdot J_{k,tot}$
I^-	$-\mathbf{n} \cdot \frac{i_{el}}{zF}$	$-\mathbf{n} \cdot \frac{1}{2}\frac{i_{el}}{zF}$	$-\mathbf{n} \cdot \frac{3}{2}\frac{i_{el}}{zF}$
I_3^-	0	$-\mathbf{n} \cdot \frac{1}{2}\frac{i_{el}}{zF}$	$-\mathbf{n} \cdot \frac{1}{2}\frac{i_{el}}{zF}$
I_2	$-\mathbf{n} \cdot \frac{1}{2}\frac{i_{el}}{zF}$	$\mathbf{n} \cdot \frac{1}{2}\frac{i_{el}}{zF}$	$\mathbf{0}$

All species flux densities vanish at the electrolyte–separator interface except for those of sodium ions.

$$\mathbf{n} \cdot \nabla[Na^+] = -\frac{\mathbf{n} \cdot \mathbf{i_{el}}}{D^{el}_{Na^+}F} - \frac{F}{RT}[Na^+]\,\mathbf{n} \cdot \nabla\Phi_{el} \tag{17}$$

2.1.1. Initial Conditions

It is necessary to define initial values for species concentrations. The total elemental iodine concentration is globally constant.

$$[I]_{tot} = [I^-] + 2[I_2] + 3[I_3^-] \tag{18}$$

Iodine is slightly soluble in water. In sodium iodide solutions, iodine is soluble in high concentrations because of triiodide formation. According to Goldstein, iodine stays in solution as long as $[Na]/[I]_{tot} < 0.476$ at 25 °C with a maximum total elemental iodine concentration of $[I]_{tot} = 11.2$ [M].[43] This correlation is valid for various degrees of dilution. Together with charge neutrality

$$[Na^+] + [I^-] + [I_3^-] = 0 \tag{19}$$

the total elemental iodine concentration and the equilibrium relation initial conditions for all species are evaluated. **Table 2** shows initial concentrations for selected total elemental iodine concentrations and C-rates. The iodine concentrations are orders of magnitude lower than the corresponding other species concentrations and only slightly change for different total elemental iodine concentrations. Initial charge concentrations for triiodide and iodine are not zero but very low for numerical stability reasons.

Table 2. Initial molar species concentrations for different C-rates and total elemental iodine concentrations for $T = 120\,°C$.

$[I]_{tot}$ [M]	$[Na^+]_0$ [M]	$[I^-]_0$ [M]	$[I^-_3]_0$ [M]	$[I_2]$ [M]
Discharging				
6	2.857	1.295	1.561	9.894×10^{-3}
8	3.809	1.724	2.085	9.928×10^{-3}
10	4.761	2.152	2.609	9.949×10^{-3}
11.2	5.333	2.409	2.923	9.958×10^{-3}
Charging				
6	5.999	5.999	2.995×10^{-4}	4.099×10^{-7}
8	7.999	7.998	3.995×10^{-4}	4.101×10^{-7}
10	9.999	9.998	4.995×10^{-4}	4.102×10^{-7}
11.2	11.198	11.198	5.595×10^{-4}	4.102×10^{-7}

**ADVANCED
SCIENCE NEWS**

www.advancedsciencenews.com

Energy Technology
Generation, Conversion, Storage, Distribution

www.entechnol.de

2.2. Charge Transport

2.2.1. Cathode Charge

The model does not resolve nanoscale processes such as double layer forming near the cathode–electrolyte surface. Local charge neutrality is enforced.

$$\frac{\partial \rho_{ed}}{\partial t} = 0 \tag{20}$$

A divergence-free current density field ensues.

$$\nabla \cdot \mathbf{i}_{ed} = 0 \tag{21}$$

Ohm's law represents the current density in the cathode domain.

$$\mathbf{i}_{ed} = -\sigma_{ed} \nabla \Phi_{ed} \tag{22}$$

Equation (21) requires several boundary conditions for solving. The electric potential at the cathode current collector is fixed at a specific value $\Phi_{cc} =$ fixed to ensure current continuity through the cathode domain. The integral current density at the cathode current collector (index cc) and electrolyte–cathode interface (index etc) must equal.

$$\int \mathbf{n} \cdot \mathbf{i}_{ed,cc} dA_{cc} = -\int \mathbf{n} \cdot \mathbf{i}_{ed,etc} dA_{etc} \tag{23}$$

A Butler–Volmer equation describes the charge transfer process between cathode and electrolyte domain. It is the standard phenomenological approach to model electrode kinetics and describes the net charge transfer rate approximating a dilute solution.[44,45]

$$i_{BV} = i_0 \left(\exp\left(\frac{\alpha_a F}{RT}\left(\Phi_{ed} - \Phi_{el} - U_{eq}([X_k])\right)\right) - \exp\left(-\frac{\alpha_c F}{RT}(\Phi_{ed} - \Phi_{el} - U_{eq}([X_k]))\right) \right) \tag{24}$$

The exchange current density results from the heterogeneous reaction kinetics at the electrolyte–cathode interface described in Equation (9). The chosen electric potential at the cathode–electrolyte interface $\Phi_{ed,etc}$ must ensure charge conservation between cathode and electrolyte.

$$i_{BV} = \mathbf{n} \cdot \mathbf{i}_{ed} = -\mathbf{n} \cdot \mathbf{i}_{el} \tag{25}$$

Assuming the activity coefficients to be 1, the Nernst equation gives reversible electrode potential for iodide–iodine reaction depending on electrolyte species concentrations (in moles).

$$U_{eq,I^-/I_2} = E^\circ_{I^-/I_2} + \frac{RT}{2F} \ln\left(\frac{[I_2]}{[I^-]^2}\right) \tag{26}$$

2.2.2. Electrolyte Charge

The electric current density field in the catholyte is divergence-free because of local charge neutrality.

$$\nabla \cdot \mathbf{i}_{el} = 0 \tag{27}$$

Concentrations and gradients of the charge-carrying species determine the electrolyte charge flux. It splits into a migration and a diffusion contribution on the lines of Equation (4).

$$\mathbf{i}_{el} = -\sigma_{el} \cdot \nabla \Phi_{el} - \sum z_k F D_k^{el} \cdot \nabla[X_k] \tag{28}$$

The ionic conductivity is

$$\sigma_{el} = \sum \frac{z_k^2 F^2}{RT} D_k^{el}[X_k] \tag{29}$$

The half-cell potential for the anode is evaluated from sodium standard potential and sodium ion concentrations at the electrolyte–separator interface.

$$U_{eq,Na^+} = E^\circ_{Na^+} + \frac{RT}{F} \ln([Na^+]) \tag{30}$$

NASICON serves as the separator material and has a high ionic conductivity. Ohm's law assuming no sodium gradient contributions to the electric potential in the NASICON represents the current density. The electric potential difference in NASICON is calculated via boundary conditions instead of discretizing charge transport equations in the NASICON in an additional computational domain.

Because of current continuity, the current densities at separator electrolyte interfaces have to be the same for both domains

$$\mathbf{n} \cdot \mathbf{i}_{el} = -\mathbf{n} \cdot \mathbf{i}_{sep} \tag{31}$$

The potential difference in NASICON thus is

$$\Delta \Phi_{sep} = -\frac{\mathbf{n} \cdot \mathbf{i}_{sep}}{\sigma_{sep} l_{sep}} \tag{32}$$

The surface unit normal vector pointing outside the related domain is **n**. **Table 3** shows important parameters for the simulation.

The external current is associated with the C-rate and the amount of energy that is stored inside the battery. The energy amount relates to the maximum and minimum sodium

Table 3. Geometry parameters and physical properties of Na–I_2 reference cell.

Parameter	Value [units]
Symmetry factors (α_a, α_c)	0.5
Cathode conductivity (σ_{cath})	2.5×10^6 S m^{-1}
Cathode length (l_c)	1 cm
Separator thickness (l_{sep})	0.5 mm
Exchange current factor (i_0°)[8]	1 A cm^{-2}
NASICON conductivity (σ_{sep})[30,48]	10 mS cm^{-1}
Diffusion coefficients Na$^+$ (D_{Na^+})[8]	6.3867×10^{-9} m^2 s^{-1}
Diffusion coefficients I$^-$ (D_{I^-})[8]	7.8625×10^{-9} m^2 s^{-1}
Diffusion coefficients I$_3^-$ ($D_{I_3^-}$)[8]	5.2677×10^{-9} m^2 s^{-1}
Diffusion coefficients I$_2$ (D_{I_2})[8]	5.9989×10^{-9} m^2 s^{-1}

**ADVANCED
SCIENCE NEWS**
www.advancedsciencenews.com

Energy Technology
Generation, Conversion, Storage, Distribution
www.entechnol.de

concentrations, which correlate with the initial concentrations and solubility limits reported earlier.

$$i_{ex} = \frac{[Na^+_{max}] - [Na^+_{min}]}{A_{ex}} \frac{CF}{3600s} V_{el} \quad (33)$$

An important parameter to describe the battery behavior is the state of charge (SOC). It sets the actual state of the battery in relation to the fully charged and discharged states.

$$SOC = \frac{\frac{\int [Na^+](x,t)dV_{el}}{V_{el}} - [Na^+]_0}{[Na^+]_{max} - [Na^+]_0} \quad (34)$$

The initial sodium concentration is usually the minimum sodium concentration enforced by the solubility limits (Table 2).

The equations were implemented in the open source software OpenFOAM, which uses the finite volume method. The solving equations are linked to the computational grid. Therefore, the solving algorithm splits and solves separately for the cathode and the electrolyte region. The two computational domains are coupled via boundary conditions. The simulations ran on an HPC system using 2 nodes and 80 cores with an average simulation time of 24 h.

3. Results

The model-predicted influences on battery performance for variations in cathode electrode design, material, and catholyte composition are presented. The simulations were conducted on a hex-dominant computational grid with approximately 1 million cells and 2.5×10^{-4} m cell size in the bulk electrolyte. Local grid refinement reduces the cell size to 30 μm in high gradient areas. The time step ranges between $\Delta t = 1$ s and $\Delta t = 10$ s depending on the C-rate. It is considerably lower in the beginning and the end of cycling to capture the larger potential changes.

At first, a simulation with a 3D geometry equivalent to the 1D geometry introduced by Zhu and Kee is conducted. The results are used to compare the spatially resolved model with the homogenized model to judge its validity. All parameters are set accordingly for the comparison. The cathode compartment is 1 mm long and contains evenly distributed carbon fibers with a specific surface area of $80\,000\,m^2\,m^{-3}$ and a porosity of 0.8. Battery cycling starts from the initial charge or discharge assuming an even distribution of species throughout the cathode domain. The initial concentrations depend on the total iodine concentration and are set to the concentration limits described in Section 2.1.1.

The current density is evaluated from the C-rate and total species concentration. **Figure 2** shows the cell voltages for two different C-rates for both models. The dashed lines represent the cell voltages extracted from Zhu and Kee, while the solid lines represent the results from the current model. The cell voltages for discharging are in good agreement. The 5 C discharge curves depart from each other at the end of discharging with the present model terminating earlier. The cell voltage for charging is lower for the present model. The decrease in cell voltage as a function of the state of charge is similar as in the model by Zhu and Kee.
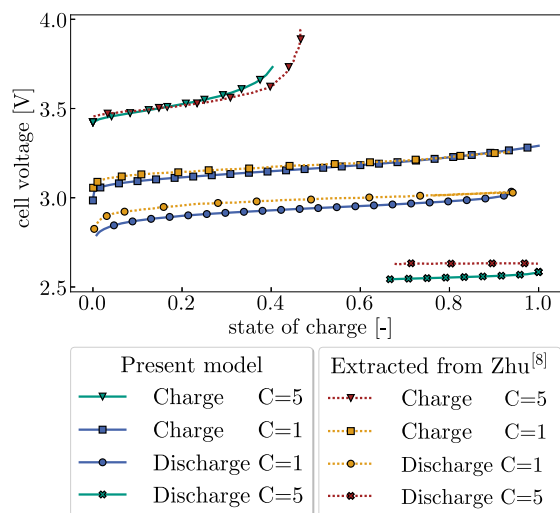

Figure 2. Comparison of a spatially resolved simulation model and a 1D simulation model introduced by Zhu and Kee.[8]

Nevertheless, the maximum relative deviation is only about 3% or 82 mV.

3.1. 3D Battery Setup

The present spatially resolved model explores several effects on the cell performance focusing on a simple cell design. The cathode electrode structure is a solid plate placed centered in the cathode half-cell. Hereby, the maximum distance between electrolyte and cathode electrode is minimal to keep diffusion paths short and prevent diffusion limitation. The shape of the disc is round with a thickness of 1 mm, a radius of 2.5 cm, and blunt edges to avoid voltage peaks at sharp corners. The material is titanium and connects to the cathode current collector with a thin wire. Titanium is a common electrode material with very high electronic conductivity and resistance to numerous chemicals. The cathode compartment is rectangular with variable distance between separator and cathode current collector and a constant length of 6 cm of the corresponding other sides.

Figure 3 shows an exemplary 3D representation of a simulated cathode half-cell. The separator is on the left side, and the current collector is on the right side. The colors of the round-shaped positive electrode highlight the Butler–Volmer current density i_{BV}. It proceeds in the cathodic direction (discharge) and is therefore negative. Red areas indicate high magnitudes of Butler–Volmer current density and, therefore, high reaction rates. The reaction rate is highest at the edge of the electrode and in the vicinity of the connection between electrode and current collector. The electrolyte region is clipped for better visibility. The colors of the electrolyte indicate electric potential, and arrows show the direction of the ionic current.

3.2. Variation of Cathode Length

The energy capacity and external current density vary strongly with the length of the cathode compartment. All simulations
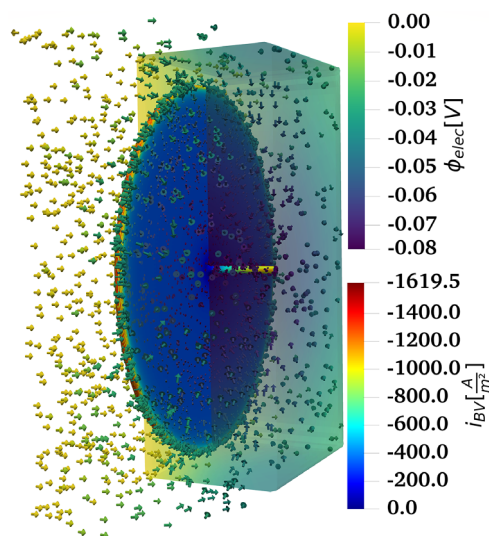
**ADVANCED
SCIENCE NEWS**
www.advancedsciencenews.com

Energy Technology
Generation, Conversion, Storage, Distribution
www.entechnol.de

Figure 3. Cathode half-cell compartment between separator (left) and cathode current collector (right). $l_c = 2$ cm, $C = 0.2$, $[I] = 8$ M.

started from equilibrium conditions. The external current density i_{ex} is 106.4 mA cm^{-2} for 1 C, 53.2 mA cm^{-2} for 0.5 C, 26.5 mA cm^{-2} for 0.2 C, and 13.2 mA cm^{-2} for 0.1 C. **Figure 4** shows cell voltages as a function of the state of charge for a cathode length of 1 cm and different C-rates. The cell voltage has a logarithmic dependence on the state of charge, which comes from the Nernst equation for equilibrium potential and plateaus as the SOC increases. The cell voltage strongly varies with the C-rate because higher current densities lead to higher electric potential gradients and, therefore, higher electrostatic potential differences in cathode $\Delta\Phi_{cath}$ and potential difference in separator $\Delta\Phi_{sep}$. The migration flux has to increase with increasing C-rate to satisfy the imposed species flux due to the relatively low diffusion flux. Therefore, the electrostatic potential
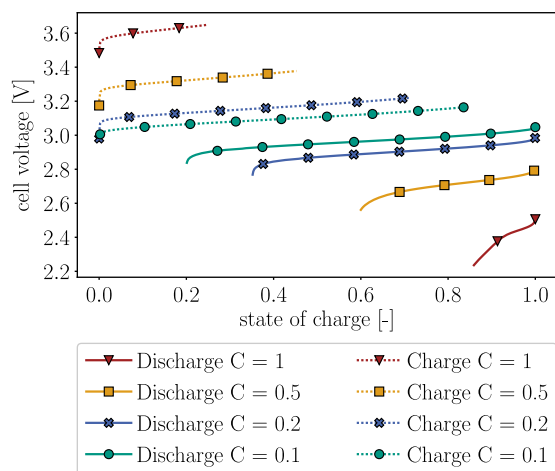
differences in electrolyte $\Delta\Phi_{el}$ must increase. A higher external current leads to a higher Butler–Volmer current between cathode and electrolyte domain and causes higher overpotentials.

Cell voltages between 0.1 and 1 C differ about 0.5 V both for charge and discharge. The achievable SOC decreases rapidly with increasing C-rate.

For discharging, SOC for 0.1 C is about 0.2 compared with only about 0.85 for 1 C. With increasing C-rate, the triiodide consumption at the cathode surface due to the Butler–Volmer reaction increases. Discharging stops when triiodide at the cathode surface is completely consumed. This diffusion-limited termination happens earlier with higher C-rates.

The coherences are similar for charging: decreasing achievable SOC with increasing C-rate. Termination occurs later than for discharging for all C-rates. Triiodide forms from iodine and iodide and due to charge conservation; the elemental iodine-to-sodium ratio decreases. Consequently, the charging process stops because precipitation of iodine would occur otherwise. For high charge rates, triiodide does not travel fast enough toward the NASICON membrane, which leads to [Na+]/[I] < 0.46 and precipitation of NaI, which causes the charging process to stop.

Figure 5 shows the same charging and discharging processes but with a cathode length of 2 cm. Therefore, the external current densities approximately double compared with the 1 cm case (218.9 mA cm^{-2} for 1 C, etc.).

The tendencies observable in the graph are similar to the 1 cm length case but with different values of cell potential. The cell voltages are nearly identical for the lowest C-rate (0.1 C) with the 1 cm cathode distance simulation. The differences in voltage increase with increasing C-rate and are up to 0.5 V for 1 C. Charging terminates shortly after the beginning for higher C-rates due to iodine precipitation. In contrast, SOC of 0.7 is achievable for 0.1 C while charging. The discharging process stops immediately when triiodide is exhausted at the cathode surface. Depletion of triiodide happens shortly after starting the discharge cycle for 0.5 C. Discharging for 1 C terminates
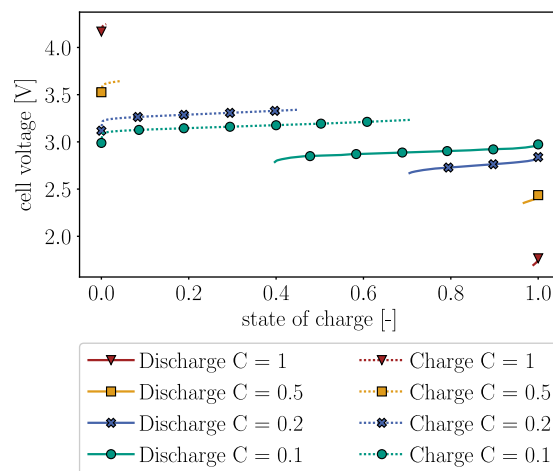

Figure 4. Cell voltage as a function of SOC for different C-rates with cathode length $l_c = 1$ cm. Dashed lines represent charging, solid lines discharging. Different colors and markers represent different C-rates ranging from 0.1 to 1 C.
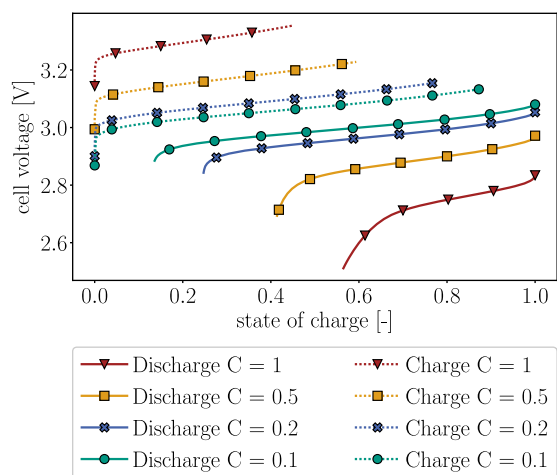

Figure 5. Cell voltage as a function of SOC for different C-rates with cathode length $l_c = 2$ cm. Dashed lines represent charging, solid lines discharging. Different colors and markers represent different C-rates ranging from 0.1 to 1 C.

**ADVANCED
SCIENCE NEWS**
www.advancedsciencenews.com

Energy Technology
Generation, Conversion, Storage, Distribution

www.entechnol.de

Figure 6. Cell voltage as a function of SOC for different C-rates with cathode length $l_c = 0.5$ cm. Dashed lines represent charging, solid lines discharging. Different colors and markers represent different C-rates ranging from 0.1 to 1 C.

because sodium-ion travel from NASICON toward the cathode current collector is too slow. Therefore, NaI precipitation occurs because Na$^+$ concentration reaches its maximum.

Figure 6 shows the charge and discharge processes for a 0.5 cm length of the cathode domain. Variations in cell voltage are lower than for 1 and 2 cm cathode lengths due to a lower external current density. The charging process terminates later. SOC is close to the theoretical maximum for 0.1 C, and the cell charges up to half of its maximum for 1 C.

The battery discharges deeply and the cell voltage barely increases for 0.1 and 0.2 C. In contrast, the achievable SOC is significantly poorer for 0.5 and 1 C, and the corresponding cell voltage drop is not negligible.

Figure 7 shows the species concentrations for the different cathode lengths. It further explains the effects of cathode length variation on the inside properties of the half-cell, which influences global performance parameters like cell voltage. The four species concentrations are exemplarily shown as a function of the dimensionless cathode length (l/l_c) for a 0.2 C discharge after 1 h. Note that iodine concentrations are significantly lower and therefore refer to the right axis to monitor their variation. The concentration gradients are generally growing with augmenting cathode length. This is a consequence of increasing external current. Therefore, the sodium flux at the NASICON separator as well as the species fluxes at the cathode electrode due to the Butler–Volmer reaction increase.

Sodium ions enter the cathode through the separator. Accordingly, the molar concentrations in the room between separator and cathode electrode (left side) are more different from the initial concentrations than in the room between cathode electrode and cathode current collector (right side). Furthermore, the Butler–Volmer reaction seems to occur mostly on the left side. The case study for the 2 cm cathode length pinpoints the discard of discharging due to diffusion limitation. Triiodide and iodine are already exhausted on the left side of the cathode electrode leaving the Butler–Volmer reaction solely to continue
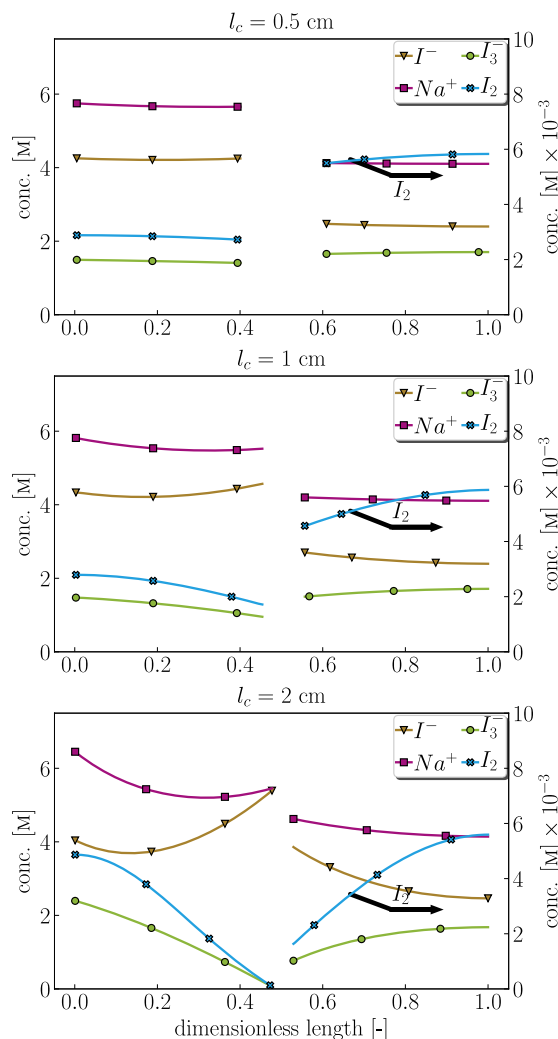

Figure 7. Concentration profiles of electrolyte species from separator (left) to cathode current collector (right).

on the right side. Subsequently, the discharge process stops when triiodide and iodine deplete on the overall cathode electrode surface because no charge-carrying species are available anymore to participate in the charge transfer reaction (Equation (3)).

Figure 8 shows the battery performance for different cathode lengths with constant external current ($i_{ex} = 501.7$ A m^{-2}). The stored energy is associated with the amount of substances. Therefore, the C-rates vary. It is salient that the cell voltages for charging are close to each other with the 2 cm case terminating earlier. In contrast, the discharge behavior of the 2 cm case differs greatly from the thinner cathode half-cells. The achievable SOC halves and the cell voltage are significantly lower.

3.3. Influence of Conductivity

Titanium serves as cathode material for the reference simulation. In addition to chemical stability against the aqueous iodine solution, the electric conductivities and the resulting influence on battery performance are among the major distinguishing
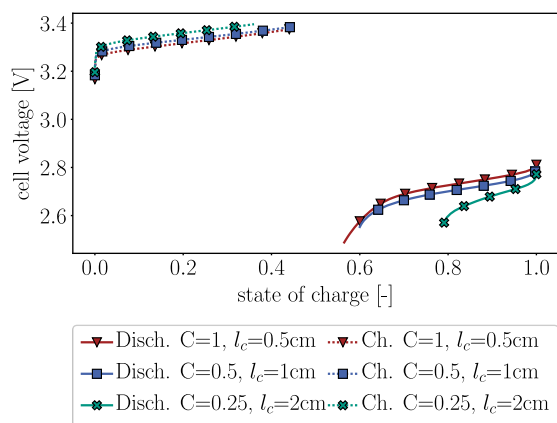
ADVANCED
SCIENCE NEWS
www.advancedsciencenews.com

Energy Technology
Generation, Conversion, Storage, Distribution
www.entechnol.de

Figure 8. Cell voltage as a function of SOC for different cathode lengths with constant external current.
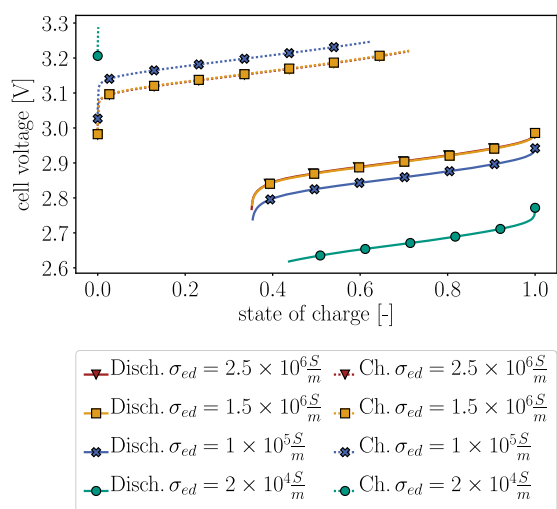

Figure 9. Cell voltage as a function of SOC for different electric conductivities of the cathode electrode with a cathode length $l_c = 1$ cm and $C = 0.2$. Dashed lines represent charging, solid lines discharging.

characteristics for cathode materials. **Figure 9** shows the effects of different electronic conductivities of cathode materials. The electric conductivity of 2.5×10^6 S m^{-1} corresponds to titanium, while 1.5×10^6 S m^{-1} and 2×10^4 S m^{-1} correspond to stainless steel and glassy carbon, which are frequently used cathode electrode materials for secondary batteries.[46,47] An arbitrary value of 1×10^5 S m^{-1} adds to this study to investigate the general influences of the electrical conductivity. The remaining battery properties are constant. The cathode length is 1 cm and the C-rate is 0.2. The cell voltage is plotted over the state of charge, and the dashed lines represent charging while the solid lines represent discharging. Different colors and markers indicate the different electric conductivities of the cathode electrode. For discharging, the cell voltage drops with decreasing conductivity. Higher electric potential gradients are necessary to deliver the same electric current, and, therefore, the potential difference $\Delta\Phi_{cath}$ increases. The cell voltages are nearly identical for conductivities of 2.5×10^6 S m^{-1} and 1.5×10^6 S m^{-1} because electric potential gradients are negligibly small for very high

conductivities. The charge curves therefore overlap. The maximum achievable SOC is about 0.35 for all electric conductivities except the lowest.

For charging, cell voltages perform similarly compared with discharging. Cell voltages for 1.5×10^6 S m^{-1} and 1.5×10^6 S m^{-1} are coincident. Charging is terminated by [Na+]/[I] falling below 0.46 and causing precipitation of iodine. Termination of battery charging takes place earlier for lower electric cathode conductivities. The low electric conductivity leads to a higher local variation in the electric potential and therefore the Butler–Volmer current. It causes a higher variation in iodine consumption and, therefore, a local exceeding of solubility limits. Furthermore, termination of charge occurs directly after the start of charging for the lowest conductivity because the Butler–Volmer reaction is driven to the cathode current collector region. Only a small surface area of connecting wire between the cathode electrode structure and the cathode current collector is available for the Butler–Volmer reaction there. Accordingly, high gradients and, therefore, high rates of iodide consumption occur.

3.4. Influence of Initial Concentrations

Figure 10 shows the influence of initial concentrations on the cell voltage for the presented battery case. The dashed lines represent charging and the solid lines represent discharging. Different colors and markers state different total elemental iodine concentrations. The cathode length is 1 cm and the C-rate is 0.2. For discharging, cell voltage decays with increasing total elemental iodine concentration because higher current densities lead to higher electric potential differences in cathode, electrolyte, and separator as well as higher overpotentials. Concentrations of 6 and 8 м terminate at SOC ≈0.35 because triiodide depletes at the cathode electrode. Concentrations of 10 and 11.2 м terminate earlier as a result of higher sodium-ion concentrations near the separator that exceed the limits of sodium iodide precipitation.
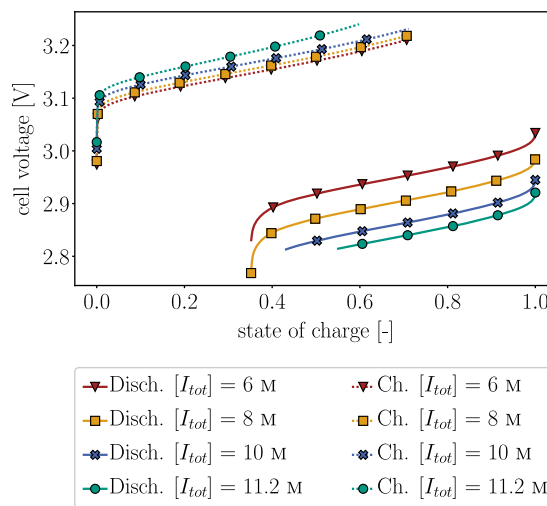

Figure 10. Cell voltage as a function of SOC for different initial species concentrations with a cathode length $l_c = 1$ cm and $C = 0.2$. Dashed lines represent charging, solid lines discharging.

During charging, cell potential differences are lower than for discharging because the overall ion concentration is higher, which leads to a higher electrolyte conductivity and, therefore, lower potential differences in the electrolyte. The charging process terminates to avoid iodine precipitation, which occurs earlier for $[I] = 11.2$ M.

4. Conclusion

To sum up, a spatially resolved simulation model of a secondary sodium–iodine battery was developed focusing on the aqueous cathode half-cell. It extends the existing 1D model by Zhu and Kee implementing it in OpenFOAM using a finite volume approach. The comparison with the 1D simulation is in good agreement and shows its validity. A preferably simple cell design is favored, and a solid plate placed in the center of the cathode compartment serves as cathode electrode. The results of the variation in cathode length show that a cathode length longer than 1 cm is undesirable because diffusion limitation effects lessen the achievable SOCs. Moreover, the simulations state that high electric conductivity of the cathode electrode is beneficial for battery performance. It predicts a negative effect on the cell potential for electric conductivities lower than $1.5 \times 10^6 \, \text{S m}^{-1}$. Operating the battery with a total elemental iodine concentration of up to 8 M is feasible without deleterious effects on the cathode half-cell. These findings add to a growing body of literature on novel liquid sodium–iodine batteries. The presented spatially resolved model is capable of dimensioning sodium–iodine batteries. Nevertheless, the conducted simulations predict poor achievable SOCs for moderate or high C-rates in combination with the simple cathode design. Therefore, future work will focus on considering more complex cathode structures to enhance overall battery performance. Further experimental investigations are necessary to verify the model-predicted conclusions.

Conflict of Interest

The authors declare no conflict of interest.

[1] T. Liu, Y. Zhang, C. Chen, Z. Lin, S. Zhang, J. Lu, *Nat. Commun.* **2019**, *10*, 1965.

[2] H. Zhu, S. Bhavaraju, R. J. Kee, *Electrochim. Acta* **2013**, *112*, 629.

[3] C. Vaalma, D. Buchholz, M. Weil, S. Passerini, *Nat. Rev. Mater.* **2018**, *3*, 18013.

[4] T. Oshima, M. Kajita, A. Okuno, *Int. J. Appl. Ceram. Technol.* **2004**, *1*, 269.

[5] M. Kamibayashi, K. Tanaka, in *2001 IEEE/PES Transmission and Distribution Conf. and Exposition*, Developing New Perspectives (Cat. No. 01CH37294) (Eds.: M. Kamibayashi, K. Tanaka), IEEE, Piscataway, NJ **2001**, pp. 1169–1173.

[6] J. Sudworth, *J. Power Sources* **2001**, *100*, 149.

[7] M. Holzapfel, D. Wilde, C. Hupbauer, K. Ahlbrecht, T. Berger, *Electrochim. Acta* **2017**, *237*, 12.

[8] H. Zhu, R. J. Kee, *Electrochim. Acta* **2016**, *219*, 70.

[9] S. Shi, J. Gao, Y. Liu, Y. Zhao, Q. Wu, W. Ju, C. Ouyang, R. Xiao, *Chin. Phys. B* **2016**, *25*, 018212.

[10] A. A. Franco, *RSC Adv.* **2013**, *3*, 13027.

[11] R. E. García, Y.-M. Chiang, W. Craig Carter, P. Limthongkul, C. M. Bishop, *J. Electrochem. Soc.* **2005**, *152*, A255.

[12] R. E. García, Y.-M. Chiang, *J. Electrochem. Soc.* **2007**, *154*, A856.

[13] G. M. Goldin, A. M. Colclasure, A. H. Wiedemann, R. J. Kee, *Electrochim. Acta* **2012**, *64*, 118–129.

[14] G. B. Less, J. H. Seo, S. Han, A. M. Sastry, J. Zausch, A. Latz, S. Schmidt, C. Wieser, D. Kehrwald, S. Fell, *J. Electrochem. Soc.* **2012**, *159*, A697.

[15] C.-W. Wang, A. M. Sastry, *J. Electrochem. Soc.* **2007**, *154*, A1035.

[16] A. H. Wiedemann, G. M. Goldin, S. A. Barnett, H. Zhu, R. J. Kee, *Electrochim. Acta* **2013**, *88*, 580.

[17] M. Kespe, H. Nirschl, *Int. J. Energy Res.* **2015**, *39*, 2062.

[18] M. Kespe, M. Gleiß, S. Hammerich, H. Nirschl, *Int. J. Energy Res.* **2017**, *41*, 2282.

[19] M. Kespe, S. Cernak, M. Gleiß, S. Hammerich, H. Nirschl, *Int. J. Energy Res.* **2019**, *43*, 6762.

[20] S. Cernak, F. Gerbig, M. Kespe, H. Nirschl, *Energy Storage* **2020**, *2*.

[21] A. Latz, J. Zausch, *ECS Trans.* **2015**, *69*, 75.

[22] A. Latz, J. Zausch, *Beilstein J. Nanotechnol.* **2015**, *6*, 987.

[23] P. W. Atkins, J. de Paula, J. Keeler, *Atkins' Physical Chemistry*, Oxford University Press, Oxford, NY **2018**.

[24] J. S. Newman, K. E. Thomas-Alyea, *Electrochemical Systems*, Wiley-Interscience, Hoboken, NJ **2004**.

[25] T. N. Andersen, *Electrochemical Kinetics. Theoretical and Experimental Aspects* (Ed: K. J. Vetter), Academic Press, New York **1967**, xxxiv + 788 pp., illus. $36, 1968.

[26] G. Milazzo, S. Caroli, *Tables of Standard Electrode Potentials*. Project of the IUPAC Electrochemistry Commission, Wiley, Chichester **1978**.

[27] *Standard Potentials in Aqueous Solution*, (Eds: A. J. Bard, R. Parsons, J. Jordan), Dekker, New York, NY **1985** (ISBN: 0-8247-7291-1).

[28] T. Liu, B. Wang, X. Gu, L. Wang, M. Ling, G. Liu, D. Wang, S. Zhang, *Nano Energy* **2016**, *30*, 756.

[29] M. M. Gross, L. J. Small, A. S. Peretti, S. J. Percival, M. A. Rodriguez, E. D. Spoerke, *J. Mater. Chem. A* **2020**, *8*, 17012.

[30] H. Fu, Q. Yin, Y. Huang, H. Sun, Y. Chen, R. Zhang, Q. Yu, L. Gu, J. Duan, W. Luo, *ACS Mater. Lett.* **2020**, *2*, 127.

[31] E. Siebert, A. Caneiro, P. Fabry, M. Levy, *J. Electroanal. Chem. Interfacial Electrochem.* **1990**, *286*, 245.

[32] J. T. Vardner, S. T. Russell, N. W. Brady, Y. Inaba, S. K. Kumar, A. C. West, *J. Electrochem. Soc.* **2020**, *167*, 20546.

[33] H. S. Wroblowa, A. Saunders, *J. Electroanal. Chem. Interfacial Electrochem.* **1973**, *42*, 329.

[34] L. M. Dané, L. Janssen, J. G. Hoogland, *Electrochim. Acta* **1968**, *13*, 507.

[35] W. K. Behl, D.-T. Chin, *J. Electrochem. Soc.* **1988**, *135*, 16.

[36] Y. Zhao, L. Wang, H. R. Byon, *Nat. Commun.* **2013**, *4*, 1896.

[37] V. A. Macagno, M. C. Giordano, A. J. Arvía, *Electrochim. Acta* **1969**, *14*, 335.

[38] D. A. Palmer, R. W. Ramette, R. E. Mesmer, *J. Solution Chem.* **1984**, *13*, 673.

[39] R. J. Kee, M. E. Coltrin, P. Glarborg, H. Zhu, in *Theory, Modeling, and Simulation*, Wiley/AIChE, Hoboken, NJ/New York, NY **2017**.

[40] A. Anderko, M. M. Lencka, *Ind. Eng. Chem. Res.* **1997**, *36*, 1932.

[41] L. Cantrel, R. Chaouche, J. Chopin-Dumas, *J. Chem. Eng. Data* **1997**, *42*, 216.

[42] L. Cantrel, J.-M. Fulconis, J. Chopin-Dumas, *J. Solution Chem.* **1998**, *27*, 373.

[43] S. W. Goldstein, *J. Am. Pharm. Assoc. Am. Pharm. Assoc.* **1952**, *41*, 333.

[44] M. Z. Bazant, *Acc. Chem. Res.* **2013**, *46*, 1144.

[45] W. Bessler, J. Warnatz, D. Goodwin, *Solid State Ionics* **2007**, *177*, 3371.

[46] S. Yamada, H. Sato, *Nature* **1962**, *193*, 261.

[47] J. N. Sweet, E. P. Roth, M. Moss, *Int. J. Thermophys.* **1987**, *8*, 593.

[48] A. Hayashi, K. Noi, A. Sakuda, M. Tatsumisago, *Nat. Commun.* **2012**, *3*, 856.